Nanofibrillar Ionic Polymer Composites Enable High Modulus Ion-Conducting Membranes

Ryan J. Fox[†], Deyang Yu[‡], Maruti Hegde[†], Amar S. Kumbhar[†, §], Louis A. Madsen[‡], and Theo J. Dingemans[†]**

[†]Department of Applied Physical Sciences and [§]Chapel Hill Analytical and Nanofabrication Laboratory, University of North Carolina at Chapel Hill, Chapel Hill, NC 27599-3050, USA

[‡]Department of Chemistry and Macromolecules Innovation Institute, Virginia Tech, Blacksburg, VA 24061, USA

KEYWORDS

Ionic liquid, polymer electrolyte membrane, ion gel, polymer, modulus, liquid crystal, composite

ABSTRACT

Polymer electrolyte membranes (PEMs) with high volume fractions of ionic liquids (IL) and high modulus show promise for enabling next-generation gas separation, electrochemical storage, and conversion applications. Herein, we present a conductive polymer-IL composite based on a sulfonated all-aromatic polyamide (sulfo-aramid, PBDT) and a model IL, which we term a PBDT-IL composite. The polymer forms glassy and high-aspect-ratio hierarchical nanofibrils, that enable fabrication of PEMs with both high volume fractions of IL and high elastic modulus. We report direct evidence for nanofibrillar networks that serve as matrices for dispersed ILs using atomic force microscopy and small- and wide-angle X-ray scattering. These supramolecular nanofibrils

form through myriad non-covalent interactions to produce a physically cross-linked glassy network, which boasts the best combination of room-temperature modulus (0.1–2 GPa) and ion conductivity (8–4 mS cm^{-1}) of any polymer-IL electrolyte reported to date. The ultra-high thermo-mechanical properties of our PBDT-IL composites provide high moduli (~1 GPa) at temperatures up to 200 °C, enabling a wide device operation window with stable mechanical properties. Together, the high-performance nature of sulfo-aramids in concert with the inherent properties of ILs impart PBDT-IL composites with non-flammability and thermal stability up to 350 °C. Thus, nanofibrillar ionic networks based on sulfo-aramids and ILs represent a new design paradigm affording PEMs with exceptionally high moduli at exceedingly low polymer concentrations. This new design strategy will drive the development of new high-performance conductive membranes that can be used for the design of gas separation membranes, and in electrochemical applications, such as fuel cells and Li-metal batteries.

1. INTRODUCTION

A growing class of solid-state polymer electrolyte membranes (PEMs) consists of ionic liquid (IL) and a polymer, combining the desirable properties of high ionic conductivity and high elastic modulus. The polymer matrix provides mechanical integrity and can serve as a matrix to ion-conducting IL domains in the case of microphase-separated systems, i.e. block copolymers (BCPs). Such PEMs are employed in myriad applications, such as solid-state Li-metal battery (LMB) electrolytes,[1] fuel cells,[2] CO_2 separation membranes,[3] electrochromic devices,[4] actuators,[5] and as gate insulators in organic thin-film transistors (OTFTs).[6] The versatility of the chosen IL, polymer, and processing strategy enable an unprecedented design space actively being explored.[7]

The potential to use PEMs in LMBs represents an enticing application that is poised to solve the issue of dendrite growth, which results in short-circuit failure and dangerous thermal runaways. Calculations and experiments show that stiff PEMs (shear modulus, G' > 1 GPa) inhibit dendrite growth, potentially enabling safe operation of LMBs.[1, 8-9] Increasing the polymer concentration in PEMs improves the mechanical properties, but usually severely degrades the ionic conductivity due to coupling of ion transport with polymer segmental motion.[10] One of the primary design objectives for PEMs is to decouple high mechanical properties and ionic conductivity.[7] Towards this end, BCPs have been extensively investigated since they can be synthetically tailored to phase separate into ion-conducting and glassy domains.[7, 11-13] However, most PEMs based on BCPs exhibit low moduli as the glassy polymer domains are weakened due to plasticization by the IL, although cross-linking the polymer in the glassy phase can inhibit such effects.[12] This approach has received significant attention and can achieve moduli on the order of 10^8 Pa with ionic conductivities at room temperature in the range of 10^{-4}–10^{-3} S cm^{-1}.[12]

Recently, Wang et al. introduced a new class of potentially revolutionary polymer electrolytes utilizing the all-aromatic sulfonated polyamide (sulfo-aramid), poly(2,2'-disulfonyl-4,4'-benzidine terephthalamide) (PBDT) and a model IL composed of 1-ethyl-3-methyl imidazolium and trifluoromethanesulfonate [Emim][TfO].[14] These PBDT-IL composites exhibit an unprecedented combination of high ionic conductivity (4 mS cm^{-1}) and modulus (3 GPa) at extraordinarily low polymer concentrations (21 wt.%) with a wide electrochemical stability window (6.1 V).[14] Such a combination of high modulus and ionic conductivity for PEMs has not been achieved with any other strategy reported in the literature and may represent a class of next-generation, high-performance PEMs. These properties are enabled by a strong physical network of rigid sulfo-aramid chains self-assembled into high-aspect-ratio helical aggregates.[14] Moreover, recent molecular dynamics (MD) simulations suggest that a complex electrostatic network of highly structured IL exist within the PBDT-IL composites due to interactions with the rigid chains possessing a high density of discrete charges along the backbone.[15] However, the microstructure and nature of these materials is not fully resolved and detailed experimental investigations are needed to direct future simulation work and elucidate design rules.

Herein, we present a comprehensive investigation of the structure and thermo-mechanical properties of PBDT-IL composites utilizing polarized optical microscopy (POM), electron and atomic force microscopy (SEM/AFM), differential scanning calorimetry (DSC), small- and wide-angle X-ray scattering (SAXS/WAXS), dynamic mechanical thermal analysis (DMTA), time-temperature superposition (TTS), and tensile strength measurements. We conclusively demonstrate that PBDT-IL composites are composed of at least two phases consisting of domains with a high (PBDT-rich) and a low (PBDT-poor) polymer concentration. We directly observe through real-space AFM and reciprocal-space SAXS measurements that high-aspect-ratio

polymer-rich fibrils form an aligned and physically cross-linked network. These fibrils form the basis of the load-bearing structure, while IL-rich domains of relatively low polymer concentration enable fast ion transport through the PBDT-IL composite. We propose that nanofibrillar self-assemblies of sulfo-aramids are key for designing PEMs with a high modulus and fast ion transport, that could lead to the design of next-generation gas separation membranes, fuel-cells, and LMBs.

2. EXPERIMENTAL SECTION

2.1 Chemicals. 1-Ethyl-3-methyl imidazolium triflate (Emim TfO) 99% was purchased from Iolitec and used as received. PBDT was synthesized with a Na^+ counterion according to previously reported literature procedures.[16-17] A yellow beige fibrillar solid was obtained, and ^{1}H NMR (Bruker 400 NB, 400 MHz, 16 scans, 25 °C) confirmed the structure and purity (see **Figure S1**). The viscosity average molecular weight was 14.7 kDa as determined by dilute solution viscometry using a suspended level viscometer in 96% sulfuric acid and using the Mark-Houwink constants for poly(*p*-phenylene terephthalamide) (PPTA).[18]

2.2 Membrane Preparation. PBDT-IL composite films were prepared by a solvent-casting method. Homogeneous solutions were prepared by dissolving dry PBDT and IL in deionized water and equilibrated at 85 °C. The mass ratio PBDT/(PBDT + IL) determines the polymer concentration in the final film. The total weight percent of PBDT and IL in the initial solution was kept constant at 4%. After complete dissolution of PBDT and IL, the homogenous clear solution was poured into a preheated flat glass dish and dried at 85 °C overnight in air. The film was further dried under vacuum at 85 °C and removed from the glass dish after 24 h.

2.3 Microscopy and Thermo-Mechanical Characterization. Optical micrographs were taken with a Nikon Microphot-FX microscope equipped with polarizing filters. Images were recorded using an OMAX 18 MP digital microscope camera and calibrated with a 0.01 mm calibration slide. Digital photographs with and without crossed polarizing film were taken with an iPhone 8 Plus. Scanning electron microscopy (SEM) was performed using a Hitachi S-4700 Cold Cathode Field Emission Scanning Electron Microscope operating at 20 kV and 11.4 mm working distance. Atomic force microscopy (AFM) topological and phase angle maps were obtained with an Asylum Research MFP3D Atomic Force Microscope. Differential scanning calorimetry (DSC) thermograms were measured with a TA Instruments DSC 2500 in aluminum pans. The samples were first heated to 200 °C to fully eliminate water and cooled at 10 °C min^{-1} until the onset of IL crystallization. The samples were held isothermally until IL crystallization was complete, to avoid cold-crystallization during subsequent heating steps. The samples were then cooled to −150 °C at 10 °C min^{-1} before measuring the thermograms at a heating rate of 2 °C min^{-1}. The crystallinity of the IL in the PBDT-IL composites was calculated by the ratio of the composite melt enthalpy to the pure IL melt enthalpy, normalized to the mass of IL within each composite membrane. The glass transition temperature (T_g) is reported as the midpoint of the transition in the heat flux vs. temperature thermograms. The T_g of PBDT-IL composites that exhibited crystallinity was measured by quenching from 200 °C to −150 °C at 200 °C min^{-1} to prevent crystallization before heating at 2 °C min^{-1}. Thermogravimetric analysis (TGA) of composite films was measured with a TA instruments TGA5500 utilizing Pt pans and a heating rate of 10 °C min^{-1} in a dry N_2 atmosphere. Dynamic mechanical thermal analysis (DMTA) was performed with a TA Instruments RSA-G2 Solids Analyzer equipped with a rectangular film clamp and forced convection oven controlled to within 0.1 °C. Dry liquid nitrogen was used as the atmosphere gas

for all measurements. PBDT-IL composite films of approximate dimensions 2 × 0.2 mm^2 and a 15 mm gauge length were affixed into the sample clamps and dried at 200 °C for 10 min under an N_2 atmosphere. After drying, the samples were cooled down to −50 °C for a 30 min isothermal hold to allow the samples to crystallize. The samples were then cooled to −150 at 5 °C min^{-1} and equilibrated for 15 min. The isochronal temperature ramps were measured at an oscillation frequency of 1 Hz and heating rate of 2 °C min^{-1}. A strain amplitude of either 0.02 or 0.1% was used below and above the T_g or T_m of the IL, respectively, both within the linear viscoelastic regime. The RSA-G2 was also used for stress-strain measurements in axial control mode at 25 °C and a Hencky strain rate of 1% min^{-1}.

2.4 X-Ray Characterization. SAXS/WAXS measurements were taken with a SAXSLab Ganesha equipped with a Cu 50 kV Xenocs Genix ULD SL X-ray Source producing an incident X-ray beam of $\lambda = 1.54$ Å and a 2D detector. Three sample to detector distances (1031, 431, and 92 mm) were used to cover the scattering vector range of $q = 4\times10^{-3}$ to 2.75 $Å^{-1}$. The total counts for each configuration was kept constant at 5×10^4, 10^6, and 2×10^7, respectively, to ensure consistency between different samples. The sample chamber was evacuated and kept at 10^{-2} mbar during measurements to avoid scattering from air. The samples were affixed to a sample holder such that only the membrane was in the X-ray beam path, thus no background subtraction was performed. For scattering measurements in the parallel configuration, the incident X-ray beam was oriented nearly parallel to the film edge. To produce 1D scattering spectra, the raw 2D scattering data were corrected for instrumental sensitivity and azimuthally averaged using software provided by SAXSLab. SasView was used to fit the 1D SAXS data using the shape-independent model function 'Correlation Length' and plotted using Igor Pro 8. The anisotropic 2D scattering patterns collected using a sample-to-detector distance of 431 mm were analyzed using the Nika package

for Igor Pro 8.[19] The polar transform of the 2D scattering data was used to plot the integrated scattering intensity over the q range 0.02 to 0.1 $Å^{-1}$ as a function of the azimuthal angle.

3. RESULTS AND DISCUSSION

3.1 Polymer Electrolyte Membranes from Supramolecular PBDT and IL. PBDT is a water-soluble, sulfonated, all-aromatic polyamide (sulfo-aramid) that forms high-aspect-ratio helical supramolecular structures in aqueous solution.[16, 20-21] These helical structures form rigid rodlike aggregates of ~0.8 nm in diameter with a persistence length of several hundred nanometers.[21] These high aspect ratio rodlike aggregates result in a lyotropic nematic liquid crystal phase at relatively low concentrations (~1 wt.%) in water,[16, 20-22] similar to other sulfo-aramids.[23-25] The chemical structures for PBDT and the IL used in this work are shown in **Figure 1A**, as in our previous publication.[14]

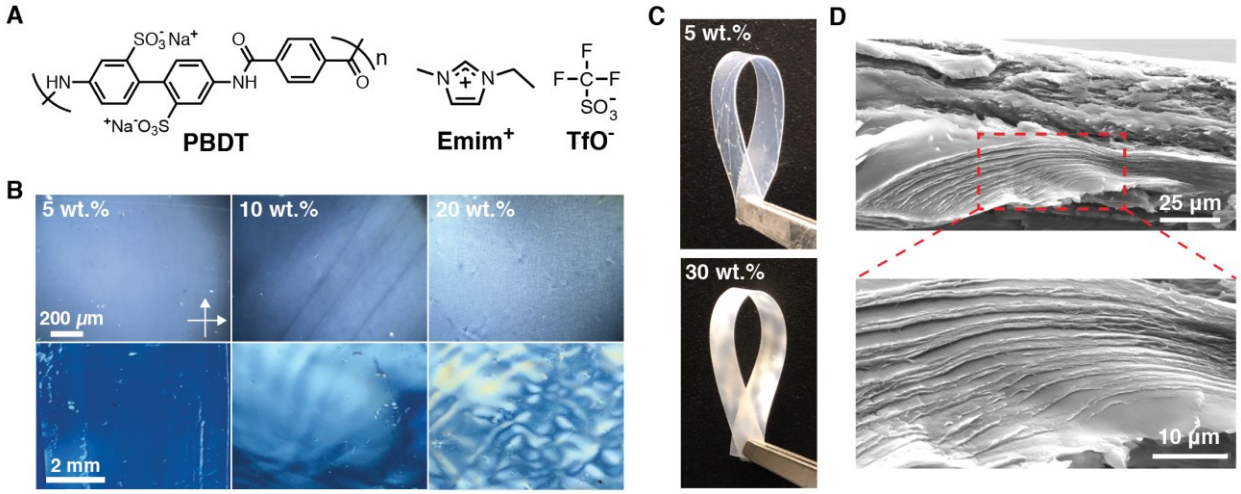

Figure 1. PBDT-IL composite membranes fabricated from the sulfonated all-aromatic polyamide, PBDT, and the IL [Emim][TfO]. **(A)** Molecular structures of PBDT and [Emim][TfO]. **(B)** Optical micrographs (*top*) and digital photographs (*bottom*) of PBDT-IL composites between crossed polarizers. The light transmittance indicates birefringence of the membranes and confirms nematic

orientational order. **(C)** Digital photographs of 5 and 30 wt.% PBDT-IL composites demonstrating the flexibility of our membranes. Multiple bending/straightening cycles can be performed manually with no apparent structural degradation. **(D)** SEM micrographs of a 30 wt.% PBDT-IL composite cross section after freeze-fracturing. The layered morphology at this composition evidences a high degree of in-plane orientation within the membranes.

Co-dissolution of PBDT and IL in aqueous solution is readily achieved with moderate heating, and the mass ratio between PBDT and IL is varied to fabricate PBDT-IL composites with different polymer concentrations. After drop-casting and water evaporation, the obtained PBDT-IL composites exhibit nematic liquid-crystalline textures, shown in **Figure 1B**, confirming liquid crystalline (nematic) orientational order of PBDT rodlike aggregates. We obtained free-standing, robust, and flexible membranes with as low as 5 wt.% PBDT that can be handled easily, demonstrated in **Figure 1C**. The PBDT-IL composites can be bent and/or twisted repeatedly without any apparent degradation in the structural integrity, suggesting strong non-covalent interactions between the PBDT and IL. Furthermore, the thermal stability of PBDT ($T_{d,95\%} \approx 500$ °C) and resulting PBDT-IL composites ($T_{d,95\%} \approx 350$ °C) are superior to any polymer-based material that is currently in use (see thermogravimetric analysis of PBDT-IL composites in **Figure S2**).

Depending on the polymer concentration used, the PBDT-IL composites are either translucent (low PBDT concentration) or semi-opaque (high PBDT concentration). This optical effect arises from the spatial heterogeneity of PBDT that exists in domains of different concentrations and the domain sizes are on the order of the wavelength of light (shown in **Section 3.2** by AFM measurements in **Figure 3**). However, as we did not apply an external field (i.e. shear or magnetic

field) during fabrication, there is no preferred global orientational order along any axis parallel to the film plane (see SAXS measurements below in **Figure 6**).

The film-drying process, where water is removed and the membrane experiences a large uniaxial dimensional change (i.e., effective compression), can however induce significant 'in-plane' alignment of semi-rigid polymers.[23, 26] The layered and hierarchical polymer morphology observed by SEM, shown in **Figure 1D** of a 30 wt.% PBDT-IL composite cross-section, suggests a high degree of in-plane orientation of PBDT within the composite membrane. The presence of IL obscures more detailed morphological observations by SEM, which would require extraction of IL with a solvent prior to imaging.[3, 27-28] Nonetheless, the clearly observable layered morphology is related to the strong local polymer orientational order and can be expected to enhance the mechanical properties of PBDT-IL composites. Moreover, this enhanced layering presents the possibility for controlled assembly of polymeric layers for separations or optical applications.

To motivate the detailed structure-property analysis in this work, we compare the mechanical properties of our PBDT-IL composites obtained at 25 °C with a compilation of the existing literature,[3, 9, 12-13, 27, 29-43] by plotting the storage modulus (E' or 3G') for a collection of PEMs/ion gels as a function of polymer concentration, as shown in **Figure 2A**.

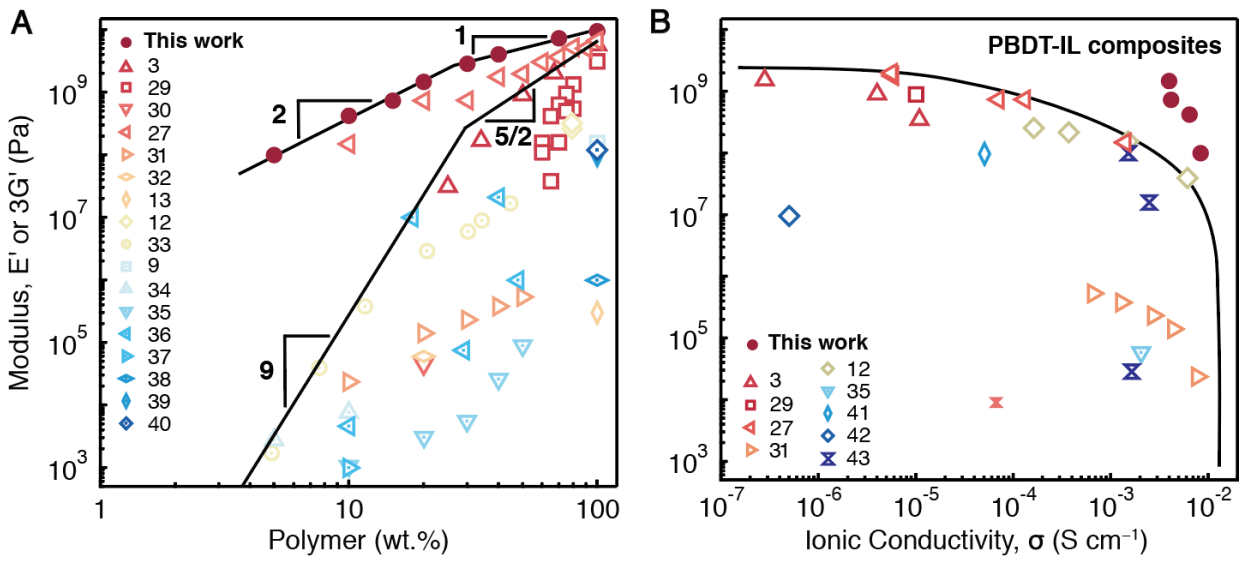

Figure 2. Comparison of PBDT-IL composites to a comprehensive literature compilation of PEMs and ion gels. The storage moduli (E' or 3G') of the PEMs/ion gels are plotted as a function of **(A)** polymer concentration and **(B)** ionic conductivity. Reference numbers are given in the figure legend. PBDT-IL composites exhibit a weak dependence (lower power law slope) of the modulus as a function of polymer concentration, enabling high stiffness at low PBDT concentration. Simultaneously, PBDT-IL composites boast high ionic conductivity combined with high moduli and outperforms all literature reports to date.

Two power laws with slopes of 5/2 and 9 represent an empirical upper bound for the majority of PEMs/ion gels reported to date, to the best of our knowledge. The strong concentration dependence of the modulus for these materials conclusively demonstrates that ILs have a strong plasticizing effect on the polymeric load-bearing components (e.g., the glassy blocks in BCPs) for PEMs reported in the literature. This results in the unfavorable requirement to use high polymer concentrations (ca. 50–80 wt.%) to obtain moduli on the order of 100 MPa or higher, which in turn reduces ionic conductivity substantially. Only two PEMs utilizing fibrillar-based polymers (i.e.,

this work (sulfo-aramid) and Mantravadi et al. using methyl cellulose), report a weaker dependence of the PEM modulus on polymer concentration (data above solid black line), scaling as 2 and 1 at low and high concentrations, respectively.[27] This demonstrates an important reinforcement mechanism that polymer fibril formation hinders the plasticizing effects of IL on the glassy, load-bearing network. However, our PBDT-IL composites outperform the ionic conductivity of cellulose-based membranes by over 2 decades in ionic conductivity at similar modulus values.

We further demonstrate the exceptional combination of mechanical and ion transport properties of PBDT-IL composites by plotting E' as a function of ionic conductivity in **Figure 2B**. In our previous report, the conductivity values for uniaxially aligned PBDT-IL composites were measured at 22 °C, parallel and perpendicular to the alignment direction.[14] The ionic conductivity parallel to the polymer alignment direction was somewhat larger than the conductivity in the perpendicular direction, and this anisotropy increases (from 1 to 3.5) as the polymer concentration increases (from 5 to 21 wt.%). For the present composites, we measured the conductivity of a few representative films in the through-thickness direction using the same apparatus and procedure as previously reported, and the conductivity values are consistent. We will report more detailed conductivity measurements of PBDT-IL composite films at elevated temperatures in a separate paper. The data included in **Figure 2B** from the wider literature range in temperature (with the lowest being 22 °C and up to 150 °C for some materials) and polymer concentration. We plot the highest values reported from each reference, so the comparisons with our 22 °C measurements are overly favorable. Again, here the solid line designates an empirical upper bound for inaccessible combinations of modulus and ion conductivity based on the current literature. The upper right corner of the graph represents an unprecedented combination of stiffness and ion transport, which is achieved alone by PBDT-IL composites. Such results strongly motivate more detailed structure-

property analysis of PBDT-IL composites undertaken in the current work and represent an alternative to the current design paradigm dominated by BCP-type PEMs.

3.2 Morphological Observations. AFM has been utilized to observe the morphology of PEMs, revealing complex microphase-separated structures. Watanabe and coworkers identified microphase-separated domains of ionic and non-ionic polyimide blocks through analysis of the surface topology (height) and phase angle (relative stiffness).[3] Similarly, we investigated the morphology of PBDT-IL composites using tapping-mode AFM, shown in **Figure 3**. The topological images, where bright and dark areas correspond to higher and lower heights, respectively, are shown in **Figure 3** (*top*). The PBDT concentration and scale bars are in the topological images. Due to changes in height differences between samples with various polymer concentrations, the height maps are not on the same absolute scale. We present the corresponding phase maps, where higher and lower phase angles are brighter and darker regions, in **Figure 3** (*bottom*). A lower phase angle corresponds to regions of higher stiffness,[44] which likely correlates with domains of higher polymer concentration.

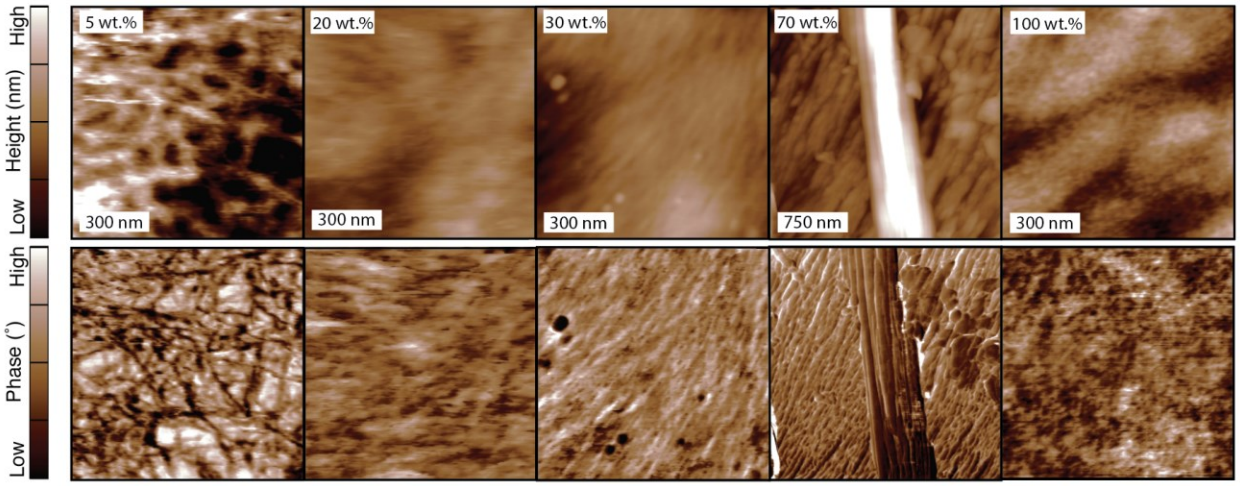

Figure 3. AFM of the PBDT-IL composite morphology. The height (*top*) and phase angle (*bottom*) maps are shown stacked for ease of comparison. The polymer concentration and scale bar are given in the topological image for each concentration. Domains of high stiffness (low phase angle) and low stiffness (high phase angle) suggest two distinct phases with different local polymer concentrations.

All of the PBDT-IL composites we investigated exhibit a heterogeneous morphology consistent with a phase-separated microstructure. At 5 wt.% PBDT, anisotropic domains with high stiffness form an interconnected network that span the observable sample. These high-stiffness domains likely contain higher PBDT concentrations than the nominal bulk concentration, i.e. local domains consisting of greater than 5 wt.% PBDT. Co-existing with these high stiffness anisotropic domains are domains of poorly defined morphology and lower stiffness, likely IL-rich domains. The observable morphology for the 5 wt.% PBDT-IL composite strongly suggests at least two distinct local environments within the composite material.

At intermediate concentrations (20 and 30 wt.%), domains of high and low stiffness are also observed, similar to the 5 wt.% PBDT-IL composite. However, the texture at 20 and 30 wt.% appears to have a distinct direction of alignment that is not readily observable at the lower

concentration. This orientational order is consistent with the nematic phase behavior observed under crossed polarizers at the micro- and macroscopic scale (see **Figure 1B).** Moreover, the domain boundaries between regions of high and low stiffness appear much more diffuse and less well-defined. These diffuse domain boundaries would suggest a decrease in polymer concentration heterogeneity.

Increasing the polymer content (70 wt.% PBDT) reveals higher-order fibrillar structures with lateral dimensions of ca. 1 um and axial lengths that traverse the entire scanned area. Upon closer inspection, these structures are composed of smaller fibrillar structures, similar to the anisotropic domains observed at lower concentrations (20-30 wt.%), on the order of 10–100 nm that evidences a complex hierarchical assembly of nanofibrillar polymer rodlike aggregates. Topological images in 3D reveal more explicitly the exquisite structure of these hierarchical fibrils (see **Figure S3**). These fibrillar structures cannot be resolved in the neat PBDT material, as there is very little stiffness contrast, and we observe a relatively uniform surface.

Our understanding of the phase morphology is represented in **Figure 4**, which depicts PBDT-rich fibrils forming a macroscopic network surrounded by PBDT-poor domains strongly coordinating with IL. To clarify, the terms ‘rich’ and ‘poor’ are relative with respect to the average value for the composite of interest, i.e., we are referring to local heterogeneities in the polymer concentration. The spatial arrangement of IL in the vicinity of PBDT chains is complex; however, we depict the positively charged [Emim] moieties strongly localized near the negatively charged sulfonic groups and the anion [TfO] localized near the hydrophobic terephthalic acid residue.[15] The transformed binary image and its corresponding 1D fast Fourier transform (FFT) intensity indicates a characteristic length scale of heterogeneous domains on the order of 100 nm. Thus, this two-phase structural model, which is phase-separated at the ~130 nm length scale, informs our

understanding towards interpreting the following thermal, scattering and thermo-mechanical results.

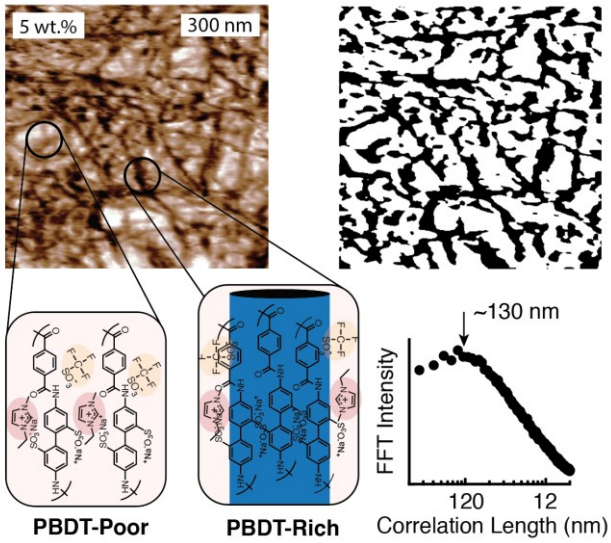

Figure 4. AFM phase angle map of a 5 wt.% PBDT-IL composite and idealized representation of the two-phase morphology, characterized by a PBDT-rich and PBDT-poor phase. The transformed binary image and corresponding 1D fast Fourier transform (FFT) intensity indicates a correlation length of ~130 nm.

3.3 Thermal Behavior. We investigated the thermal behavior of PBDT-IL composites with DSC to confirm the two-phase morphology observed via AFM. Thus, after complete elimination of water and cooling down to −150 °C, we show the heating thermograms (2 °C min^{-1}) for neat IL and PBDT-IL composites in **Figure 5A**. To investigate the crystallization of IL within the PBDT-IL composites, samples were allowed to fully crystallize during the cooling step prior to measurements.

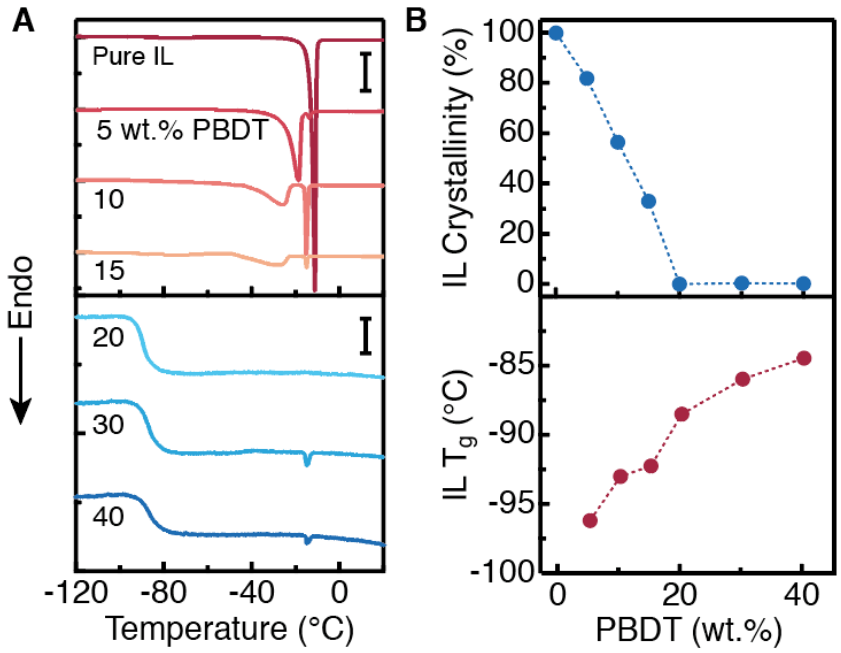

Figure 5. DSC characterization of PBDT-IL composites. **(A)** Thermograms of the 2nd heat measured for neat IL (i.e. 0 wt.% PBDT) and PBDT-IL composites with up to 40 wt.% PBDT. The heat flux vertical scale bars are 50 mW g^{-1} (*top*) and 5 mW g^{-1} (*bottom*) given in the figure. The melt endotherm peak splitting observed at 5, 10, and 15 wt.% PBDT indicates the coexistence of two local environments for the IL. **(B)** (*top*) Calculation of the IL crystallinity from total melt enthalpy for the PBDT-IL composites as a function of PBDT concentration, assuming the neat IL is 100% crystalline. The IL crystallinity is eliminated at 20 wt.% PBDT, while higher PBDT concentrations result in composites with negligible crystallinity. (*bottom*) T_g measured on the 2nd heat of samples after quenching to −150 °C at a cooling rate of 200 °C min^{-1}. The glass transition increases nearly linearly with PBDT concentration, before beginning to plateau.

The neat polymer does not exhibit any measurable thermal transitions, i.e., T_g or T_m, as detectable by DSC up to its degradation temperature. However, the morphology of PBDT-IL composites can be elucidated by analysis of the changes in phase transitions related to the IL in

the presence of PBDT. The IL melt endotherms in PBDT-IL composites containing between 5–20 wt.% PBDT is shifted to temperatures below the T_m of the pure IL and splits into two distinct endotherms, shown in **Figure 5A**. The two peak temperatures and shapes are sensitive to the concentration of PBDT, and strongly suggests that the IL experiences two distinct local environments. As a means of comparison, water within a hydrophilic polymer matrix exhibits multiple melt peaks depending on the degree of confinement and the strength of its interaction with the polymer.[45-47] The assignment of melt peaks is made more complicated by the fact that cation exchange of Na^+ with $Emim^+$ can occur between PBDT and IL.[14-15] We doped small amounts of [Na][TfO] into [Emim][TfO] and observed that the resulting crystal melt endotherms were of lower melt enthalpy and shifted to slightly lower temperatures compared to the pristine IL (see **Figure S4**).

We approximate the degree of IL crystallinity in the PBDT-IL composites by taking the ratio of the melt endotherms of the composites to the neat IL (assuming 100% crystallinity of the neat IL), shown in **Figure 5B** (*top*). The decrease in crystallinity with PBDT concentration is nearly linear, with a ~5% crystallinity decrease per wt.% PBDT added. Above 20 wt.% PBDT, we observe only a small degree of crystallinity (<1%) and a prominent T_g associated with the IL near −90 °C. These results demonstrate the ability of PBDT to inhibit IL crystallization, suggesting a significant reduction in IL mobility.

To confirm the synergistic interactions between PBDT and IL on the IL dynamics within the composite, we measured the IL T_g of wholly amorphous (non-crystallized) composites obtained by quenching the samples from 200 °C to −150 °C at 200 °C min^{-1}, which prevented IL crystallization (see **Figure S5**). We show the T_g as a function of PBDT concentration in **Figure 5B** (*bottom*), which increases monotonically with PBDT concentration from −97 to −83 °C. This

increase in T_g demonstrates compatibility between the charged PBDT and IL that restricts the mobility of the IL and is consistent with recent MD simulations.[15]

3.4 SAXS/WAXS Characterization. We employed SAXS to characterize the polymer structure within the PBDT-IL composites to complement our surface-based AFM measurements. The orthorhombic membrane geometry dictates that two scattering configurations are used to fully characterize the polymer structure and orientational distribution.[48] First, we orient the incident X-ray beam parallel to the surface normal, depicted in **Figure 6A**, which causes the scattering vector (q) to be located within the x-y plane.

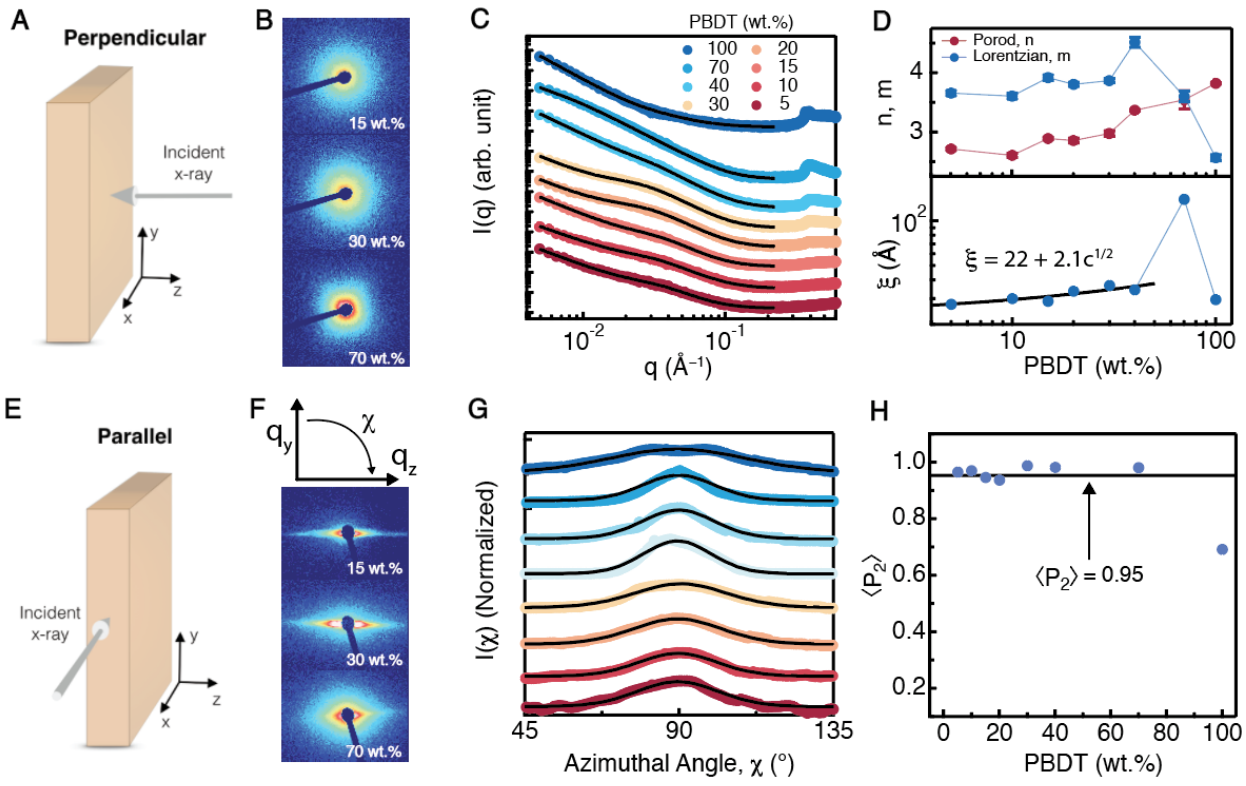

Figure 6. SAXS analysis of PBDT-IL composites. **(A)** The perpendicular scattering configuration, where the incident X-ray is parallel to the film normal, probes spatial correlations in the x-y plane. **(B)** Representative 2D SAXS patterns of the low-q region for 15, 30, and 70 wt.% PBDT-IL

composites. The isotropic scattering intensity distribution confirms that the nematic domain directors have no significant macroscopic orientation with respect to the x- or y-axis. **(C)** 1D SAXS intensity as a function of q for the PBDT-IL composites with 5 to 100 wt.% polymer (bottom to top). The intensity spectra have been vertically offset for clarity. Solid lines are fits with a correlation length model given by **Eqn. 1**. **(D)** Concentration dependence of the Porod exponent (n), Lorentzian exponent (m), and correlation length (ξ) obtained from fitting the 1D SAXS data. **(E)** The parallel scattering configuration, where the incident X-ray is parallel to the film surface, probes spatial correlations in the y-z plane. **(F)** 2D SAXS patterns for PBDT-IL composites in the parallel configuration and schematic illustrating the azimuthal intensity dependence. Strongly anisotropic scattering is observed for all PBDT-IL composites, indicating a high degree of in-plane polymer nanofibril orientational order. **(G)** Scattered intensity distribution along the azimuthal angle (χ) over the q range of 0.01 to 0.08 $Å^{-1}$. The solid lines are fits to the data using a Maier-Saupe type distribution given by **Eqn. 2**. Colors and concentrations are the same as in **(C)**. **(H)** Order parameter $\langle P_2 \rangle$ calculated from numerical integration of **Eqn. 3** as a function of PBDT concentration. The average order parameter for all composites is 0.95 ± 0.03, indicating high orientational order of PBDT fibrils. Error bars for individual values are smaller than the markers.

The 2D intensity pattern from SAXS measurements in the perpendicular scattering configuration are shown in **Figure 6B** for a select set of PBDT-IL composites. The scattered intensity is isotropic at all PBDT concentrations, indicating a random orientational distribution of polymer chains in the x-y plane averaged over the illuminated volume from the X-ray beam diameter (~1 mm) and sample thickness. We emphasize that the observed isotropy here does not conflict with the aligned texture observed in AFM images presented earlier, as SAXS is a bulk-averaged technique and AFM is inherently microscopic and surface level. The azimuthally averaged 1D intensity as a

function of q is given in **Figure 6C** and vertically offset for visual clarity. We fit the 1D SAXS intensity for the PBDT-IL composites with a shape independent correlation length model in SasView over the q range 0.004 to 0.2 Å^{-1}, given by **Eqn. 1**:

$$I(q) = \frac{A}{q^n} + \frac{B}{1+(q\xi)^m} + I_{inc} \quad \textbf{(1)}$$

where the first term describes a Porod law with amplitude A and exponent n, and the second term is a Lorentzian correlation decay with amplitude B, correlation length ξ, and exponent m. The additive parameter I_{inc} accounts for the incoherent background scattering. The fits are shown as the solid lines in **Figure 6C** and the model agreement with the data is excellent. The corresponding fitting parameters of n, m, and ξ are shown in **Figure 6D** as a function of polymer concentration. With increasing polymer concentration, n increases from 2.7 at 5 wt.% to 3.8 at 100 wt.% PBDT. Using a mass fractal theoretical framework, the increasing power law exponent suggests a denser network structure of polymer chains with higher polymer content.[49] We interpret the Lorentzian feature as arising from the cross-section of rodlike aggregates within higher order PBDT-rich fibrillar structures. The Lorentzian exponent m is weakly dependent on the polymer concentration, with values fluctuating between 3.5 and 4.5 for all materials except the pure polymer. These values are close to 4, which would suggest that the nanofibrillar aggregates have a well-defined interface, irrespective of the IL concentration.[50] We fit the concentration dependence of the correlation length ξ of the PBDT-IL composites, below 70 wt.% PBDT, with a power law and baseline offset, giving an extrapolated zero-concentration correlation length of ~22 Å. We speculate that this represents the limiting value of the nanofibril lateral dimension after mixing IL with an aqueous PBDT solution. The correlation length increases weakly with polymer concentration over this concentration range scaling as $\xi \sim c^{1/2}$. This result suggests that the constituent nanofibrils within

the PBDT-IL composites increase in diameter with higher PBDT concentration and are highly resistant to complete solubilization by IL.

The uniaxial deformation experienced by the polymer fibrils during the drying process induces a significant amount of in-plane orientation producing a highly layered structure (**Figure 1D**). The parallel scattering configuration, also referred to as 'edge-on', probes this alignment by placing the incident X-ray beam nearly parallel to the film surface, as illustrated in **Figure 6E**. The anisotropic azimuthal angular dependence of the scattered intensity projected on the y-z plane in reciprocal-space, shown in **Figure 6F**, is related to the in-plane orientational distribution of PBDT fibrils. We quantify the orientational order by fitting the azimuthal intensity distribution with a Maier-Saupe type distribution, given by **Eqn. 2**:

$$I(\chi) = I_0 + A\, exp[\alpha\, cos^2(\chi - \chi_0)] \qquad \textbf{(2)}$$

where I_0 is the isotropic baseline, A is the scattering amplitude, α is an anisotropy factor related to the width of the intensity distribution, and χ_0 is the azimuthal angle of the peak.[51] The azimuthal intensity distributions, normalized and vertically offset for visual clarity, and corresponding fits using **Eqn. 2** is shown in **Figure 6G** for all PBDT-IL composites studied here. Using the α values obtained from fitting the azimuthal intensity distributions, the fibril alignment is calculated through the order parameter, $\langle P_2 \rangle$, via numerical integration of **Eqn. 3**:

$$\langle P_2 \rangle = \frac{\int_{-1}^{1} exp[\alpha\, cos^2(\beta)]\, P_2(cos\beta)\, dcos(\beta)}{\int_{-1}^{1} exp[\alpha\, cos^2(\beta)]\, dcos(\beta)} \qquad \textbf{(3)}$$

where $P_2(cos\beta) = \frac{1}{2}[3\, cos^2(\beta) - 1]$ is the second-order Legendre polynomial coefficient (also known as the Hermann's orientation function). A $\langle P_2 \rangle$ value of unity indicates perfect orientation, while a value of zero corresponds to an isotropic orientational distribution. The calculated $\langle P_2 \rangle$ values for the PBDT-IL composites is given as a function of polymer concentration in **Figure 6H**.

A $\langle P_2 \rangle$ value near 0.7 is calculated for neat PBDT, in agreement with previous studies of supramolecular sulfo-aramids.[23] The alignment for PBDT-IL composites appears to be invariant with concentration, with an average $\langle P_2 \rangle$ of 0.95 ± 0.03, indicating near perfect orientation of PBDT fibrils in-plane of the film. This value is in agreement with the expected orientational order calculated using an affine deformation model under uniaxial deformation (analogous to the film-drying process), which asymptotically approaches 1 at large strains.[51] Clearly, by the high value of $\langle P_2 \rangle$ and its concentration independence, the orientational order of PBDT fibrils within the composites is close to the maximum attainable using a solution-casting method.

Further structural details, reporting on both polymer and IL spatial correlations, can be elucidated by analysis of the high-q scattering of PBDT-IL composites using WAXS. We show the 1D scattering intensity in the perpendicular configuration, arbitrarily vertically offset for visual clarity, in **Figure 7** for the neat IL, neat PBDT, and resulting PBDT-IL composites and the scattering features are summarized in **Table 1**.

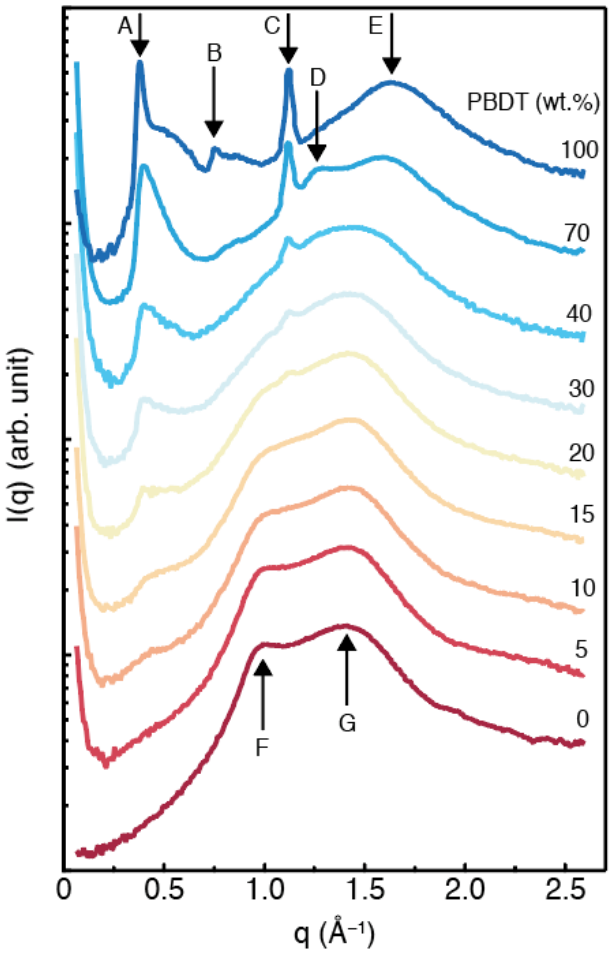

Figure 7. WAXS spectra of neat PBDT, PBDT-IL composites, and neat IL measured in the perpendicular configuration. The ordinate is log-scale and the intensity spectra have been arbitrarily vertically offset for clarity. The scattering features are marked with arrows in the figure and are tabulated in **Table 1**. Features originating from the polymer increase in intensity with polymer concentration. The pure IL has a double-topped feature that dominates the scattering below 20 wt.% PBDT.

Table 1. Tabulated peak positions of WAXS analysis, corresponding d-spacings from Bragg's Law, and assignment of their structural origin. The scattering feature that is not common to either the neat polymer or neat IL is shaded in grey.

Peak	q* (Å^{-1})	2π/q* (Å)	Assignment
A	0.38	16.5	PBDT 001
B	0.75	8.4	PBDT 002
C	1.12	5.6	PBDT 003
D	1.29	4.9	PBDT-IL-PBDT
E	1.64	3.8	PBDT-PBDT
F	1.00	6.3	IL Correlation
G	1.41	4.5	IL Correlation

The X-ray diffraction peaks for neat PBDT have been assigned previously[14, 16, 20-21] and are summarized here. Peaks located at q = 0.38 Å^{-1} (**A:** 16.5 Å), 0.75 Å^{-1} (**B:** 8.3 Å) and 1.12 Å^{-1} (**C:** 5.6 Å) correspond to the polymer repeat unit 001, 002, and 003 reflections, characteristic of nematically aligned sulfo-aramids.[23] Local π-π packing of amorphous all-aromatic PBDT chains yields a broad peak centered at q = 1.64 Å^{-1} (**E**: 3.8 Å). As the polymer concentration increases within the PBDT-IL composite, the features associated with the polymer increase in intensity, and vice-versa.

The neat IL displays two prominent correlation peaks, which present as a double-topped feature with maxima at q = 1.00 Å^{-1} (**F:** 6.3 Å) and 1.41 Å^{-1} (**G:** 4.5 Å). The double-topped feature builds in as the concentration of polymer is reduced and dominates the scattering spectra for composites with less than 20 wt.% PBDT. We assign peak F as [Emim]-[Emim] correlations by measuring IL samples doped with [Na][TfO], which reduces the intensity of peak F (**Figure S6**). More detailed analysis of the local structure of the IL is out of the scope of the current work.

The only peak that is observed in the PBDT-IL composites WAXS spectra which is not common to either neat PBDT or IL is peak D, at q = 1.29 Å^{-1} (**D:** 4.9 Å), see **Table 1**. Only two PBDT-IL composites, 70 and 40 wt.%, exhibit this scattering feature as a small, broad peak. We propose that

this scattering peak corresponds to a population of PBDT chains with an expanded π-π distance due to coordination with the IL. Direct insertion of an imidazolium ring between two benzene rings in mixtures of 1-dodecyl-3-methylimidazolium bis(trifluoromethanesulfonyl)amide ($[C_{12}mim^+][TFSA^-]$) and benzene causes an increase in the π-π distance from 3.3 to 7.5 Å.[52] In PBDT-IL composites, the coordination of the imidazolium cation with the PBDT chains may not be a direct insertion between the aromatic rings of PBDT. Instead, we speculate that the coordination and partial insertion of [Emim] with PBDT expands the inter-aromatic distance of PBDT from 3.8 to 4.9 Å. For the 70 wt.% PBDT-IL composite, both the 4.9 and 3.8 Å correlation distances are clearly observed. This confirms that there are two distinct local environments within the PBDT-IL composites, consisting of either strongly coordinated or uncoordinated PBDT chains with IL. This peak, which may be present at lower PBDT content but obscured by the pure IL peaks, likely reports on local IL-polymer interactions that could contribute to the formation of a collective electrostatic network proposed to be important for PBDT-IL composites.[14-15]

3.5 Thermo-Mechanical Characterization. The mechanical properties of PEMs are of utmost importance for their envisioned use as gas separation membranes or solid-state battery electrolytes. Moreover, detailed analysis of the thermo-mechanical response of polymer PEMs can provide information on their local- and long-range dynamics and phase behavior. We used DMTA to characterize the mechanical properties of PBDT-IL composite films as a function of temperature. The storage (E') and loss (E") moduli, measured isochronally at 1 Hz from −150 to 350 °C, is given in **Figure 8A** for four PBDT concentrations.

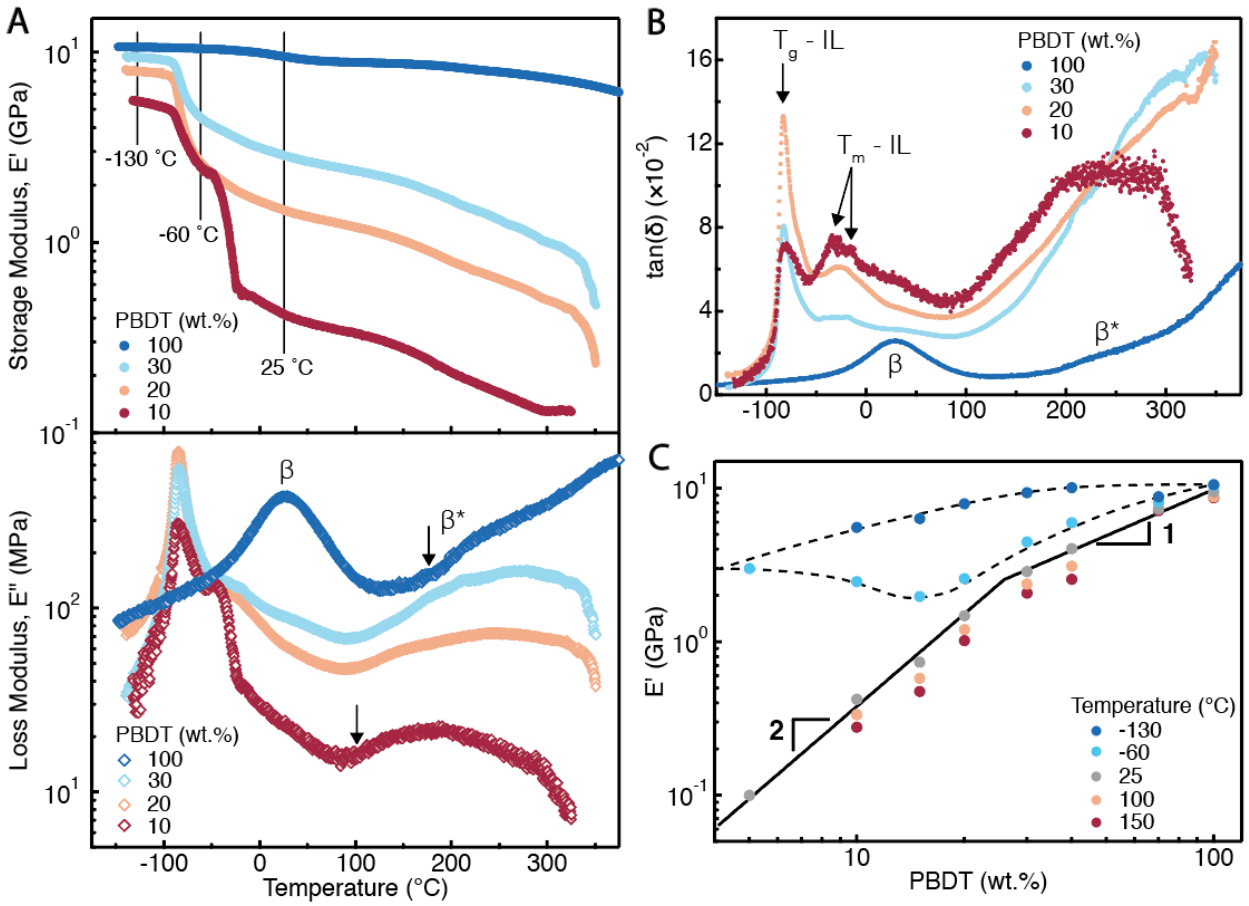

Figure 8. Isochronal DMTA results of PBDT-IL composites. **(A)** Storage (E', *top*) and loss (E'', *bottom*) moduli as a function of temperature measured at 1 Hz with a heating rate of 2 °C min^{-1}. Temperatures are indicated in the figure by vertical lines where storage modulus scaling relationships are extracted. Dispersion peaks arising from secondary polymer relaxations, designated as β and β*, are labeled on the E'' curve. The onset of the β* relaxation is shifted to lower temperatures with higher IL concentration, indicated by the arrows. **(B)** Isochronal loss tangent as a function of temperature for PBDT-IL composites. The IL T_g is evident as a sharp, prominent peak near −90 °C. Dispersion peaks due to the dual IL crystal melting event for 10 wt.% PBDT are marked with arrows. (**C**) Storage modulus as a function of PBDT concentration at −130, −60, 25, 100, and 150 °C. Solid lines are power law fits to the data and dashed lines are guides to

the eye. A transition in power law scaling from 2 to 1 occurs between 20 and 30 wt.% PBDT. The extrapolated modulus to zero PBDT concentration at −130 and −60 °C is 2–3 GPa.

The neat polymer exhibits a E' of ~10 GPa at cryogenic temperatures, and maintains its high stiffness up to extreme temperatures of >350 °C. These exceptional thermo-mechanical properties, characteristic of aramids, bestows PBDT with ideal characteristics as a matrix material for fabrication of high-performance PEMs. Two main relaxation processes are evident in the neat polymer by inspection of E", with a β-relaxation centered near 25 °C and a β*-relaxation appearing as a broad shoulder with an onset temperature near 200 °C. The β- and β*-relaxations have been attributed to complex motions of the amide bond and ring flips from the main-chain aromatic groups, respectively, and are characteristic of aramid secondary thermal relaxations.[53]

The PBDT-IL composites between 10 and 30 wt.% PBDT possess E' values between 5–10 GPa at −130 °C, but experience a significant drop in their stiffness over the range of −130 to −60 °C. This decrease in stiffness is primarily due to the T_g of IL as evidenced previously via DSC measurements. The observed loss peak associated with this transition is intense and narrow. Inspection of the loss tangent, presented in **Figure 8B**, indicates that the most intense IL transition is observed at 20 wt.% PBDT. Thus, the 20 wt.% PBDT-IL composite has the highest concentration of amorphous, glassy IL that results in the most significant mechanical decrease over the T_g of the IL.

At temperatures higher than the IL T_g, the E' for 20 and 30 wt.% PBDT-IL composites maintain a relatively constant value over the temperature range of −60 to 150 °C. This behavior is consistent with a physical network of glassy polymer chains providing mechanical integrity to the composite. At higher temperatures, the onset of the β*-relaxation causes a slight decrease in the stiffness. The

β*-relaxation precedes complete decomposition of the IL above ~300 °C, resulting in mechanical failure of the PBDT-IL composites. In contrast, the 10 wt.% PBDT-IL composite experiences a significant and sudden drop in E' from −50 to −10 °C arising from the melting of IL crystals. The IL crystal dual-melting endotherm, observed in DSC experiments, can also be confirmed by inspection of the loss tangent of the 10 wt.% PBDT-IL composite, indicated by the two arrows (**Figure 8B)**.

To determine the effective modulus of crystalline IL, we plot the decrease in E' from −50 to −10 °C as a function of IL crystallinity (**Figure S7**). The linear slope, 2.0 ± 0.6 GPa, extracted from fitting these data is an estimate of the effective modulus of IL crystallites. This value is in agreement with recent rheological measurements of imidazolium-based ionic liquids, which reports a glassy modulus of ~1 GPa.[54-56] This is the first measured value of the modulus of crystalline IL within a PEM and suggests that IL-rich regions form a percolated network throughout the material.

We analyze the role of PBDT in the reinforcement of the composite by plotting E' as a function of PBDT concentration at various temperatures corresponding to different IL structures within the material (**Figure 8C**). At −130 °C, the IL is glassy and/or semi-crystalline, depending on the specific polymer concentration as shown by DSC (**Figure 5**). At −60 °C, the amorphous IL is above its T_g and bestowing liquid-like mobility but is still below the T_m of the IL crystal, resulting in the small decrease in E' up to 20 wt.%. The two trends in E' at −130 and −60 °C, when extrapolated to zero polymer concentration, converge on a value of ~2 GPa (dashed lines in **Figure 8C**) representing the effective modulus of the crystalline IL, as shown above. Finally, at 25 °C the IL is above both the T_g and T_m, exhibiting liquid-like behavior at all concentrations. At 25 °C, the IL appears to have a negligible individual contribution to the mechanical properties of the

composite; thus, the E' scaling at 25 °C reports on the morphology and structure of the PBDT network alone.

The E' concentration scaling of the PBDT-IL composites at 25 °C follows two power law regimes, which intersect between 20 and 30 wt.% PBDT. At low concentrations, E' follows a power law of exponent 2, while at high concentrations the E' scaling is linear. Below 30 wt.% PBDT, the modulus power law scaling exponent 2 is consistent with the expected value from considerations of polymer interactions mediated through chain entanglements.[57] In contrast, the linear scaling of E' at high polymer concentrations is consistent with the expected trend of continuous fiber reinforced composites as described by the linear rule of mixtures.[48] Here, mesoscopic percolated PBDT-rich fibrils may act as a self-reinforcing network that mechanically supports the IL-rich domains. Our SAXS data indicates a smooth transition in structural characteristics at the length scales of <50 nm over this concentration range. Thus, we speculate that the cross-over in E' scaling likely corresponds to a critical mesoscopic network connectivity which enables rule of mixtures type behavior (linear E' scaling).

We have shown through DSC and AFM analysis that PBDT-IL composites consist of a structure with at least two microphase-separated domains, one PBDT-poor (IL-rich) and another PBDT-rich (IL-poor). With this model of the PBDT-IL composite morphology, we show in **Figure 9A** an idealized isochronal E" temperature scan with decomposed contributions from PBDT-rich and PBDT-poor domains arising from secondary polymer relaxations with the IL T_g superimposed near −85 °C. Experimentally, we find evidence for this structural model through analysis of the E" temperature dependence, where all concentrations are shown, vertically offset for visual clarity, in **Figure 9B**.

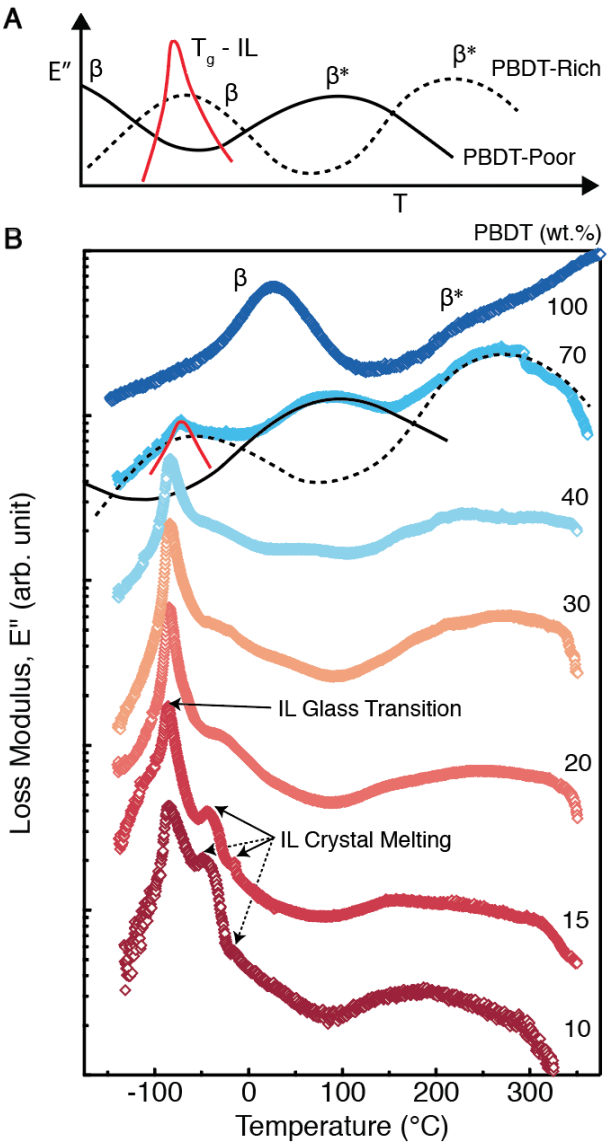

Figure 9. Analysis of the thermo-mechanical relaxations of neat PBDT and PBDT-IL composites. **(A)** Idealized isochronal E" as a function of temperature at 1 Hz for PBDT-IL composites decomposed into contributions from the amorphous IL, PBDT-rich, and PBDT-poor domains. **(B)** Experimental E" temperature dependence at 1 Hz for neat PBDT (dark blue) and PBDT-IL composites (concentrations given in figure) vertically offset for visual clarity. Black solid and dashed lines on the 70 wt.% sample represent the relaxation features originating from PBDT-poor

and PBDT-rich domains, respectively. The red line and arrows indicate features originating from the crystal melting and glass transition of IL.

Due to the presence of two distinct polymer phases (PBDT-poor and PBDT-rich), we observe a superposition of polymer secondary relaxations, illustrated by the solid and dashed lines in **Figure 9B**. Such a superposition of two secondary loss peaks has been observed previously in microphase-separated sulfonated polyimide PEMs.[3] The polymer contained in the PBDT-poor phase is highly plasticized through coordination with IL, shifting the entire relaxation temperature profile to lower temperatures and broadening the E" dispersion peaks.

The superposition of secondary relaxations is most evident in the 70 wt.% PBDT-IL composite. The broad E" peak between 0 and 150 °C for the 70 wt.% PBDT sample arises from the β*-relaxation process occurring in the PBDT-poor domains. This feature can be seen to systematically grow in intensity with increasing PBDT concentration in the composites, and is absent in the neat polymer. We do not observe an E" feature associated with the β-relaxation of the PBDT-poor, suggesting that this relaxation is below the accessible experimental temperature range.

The PBDT-rich secondary relaxations are more prominent in the E" signal because these polymer-rich domains constitute the primary load-bearing structure in the PBDT-IL composites. We observe a clear shift in the 'β* - PBDT-rich' relaxation to lower temperatures as the polymer concentration is reduced. This trend indicates that increasing the IL concentration plasticizes the local dynamics of the PBDT chains to some extent. The low-temperature 'β - PBDT-rich' relaxation is similarly shifted to lower temperatures when compared to the β-relaxation of the neat PBDT. However, this relaxation is dominated by the T_g of the IL and is strongly obscured. From

these data, we conclude that there exists a broad relaxation feature in all composites near the IL T_g, likely originating from the β-relaxation within the PBDT-rich domain.

3.6 Time-Temperature Superposition. To further probe the secondary polymer relaxations and IL glass transition observed in isochronal DMTA measurements, we utilize time-temperature superposition (TTS) to construct master curves for the neat polymer and PBDT-IL composites with 20, 30 and 40 wt.% PBDT at a reference temperature T_{ref} = −90 °C, shown in **Figure 10A**. Over the temperature range used for the master curve construction, we successfully applied TTS and no vertical shift factors were used. For the PBDT-IL composites, temperatures higher than −50 °C resulted in a breakdown in TTS, and we omitted those data in our analysis. We observed high frequency tails to the E" data, likely due to the very high material stiffness and small amplitude strains used (<0.1%).

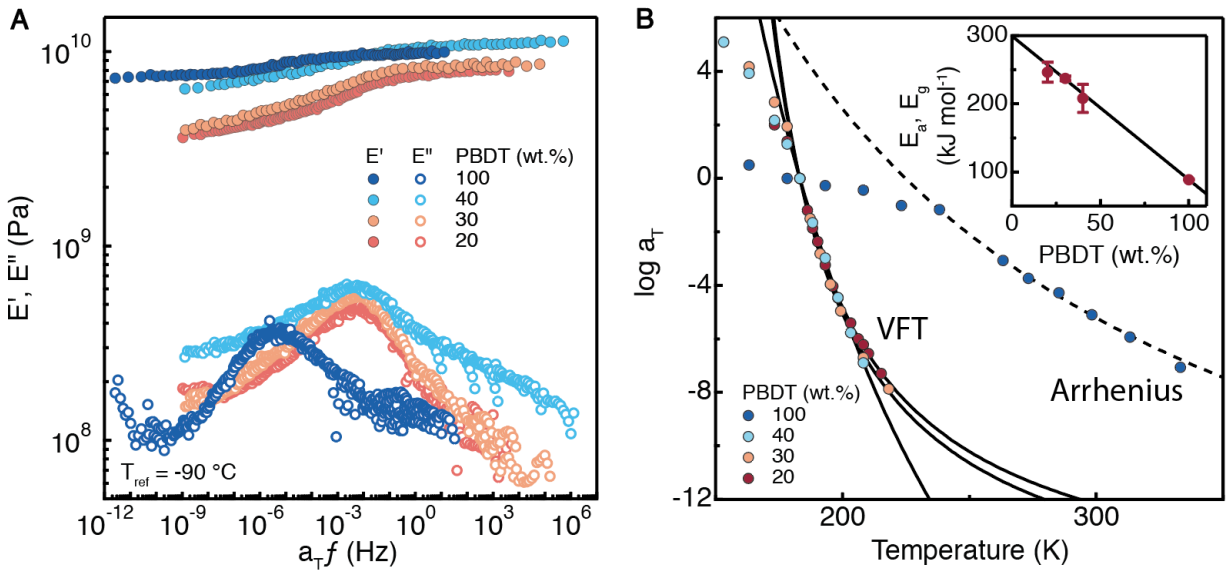

Figure 10. TTS analysis of PBDT-IL composites. **(A)** Master curves of E' (filled symbols) and E" (open symbols) at T_{ref} = −90 °C. **(B)** Logarithm of shift factors used in TTS as a function of absolute temperature. Dashed line is a fit to the Arrhenius equation (**Eqn. 4**) for the neat PBDT

and solid lines are fits to the VFT law (**Eqn. 5**) for the PBDT-IL composites. **(Inset)** Arrhenius activation energy (E_a) and VFT apparent activation energy (E_g) for neat PBDT and PBDT-IL composites, respectively. Solid line is a linear fit to the data.

For neat PBDT, the main transition we observe is the β-relaxation centered at 25 °C (see **Figure 8**). Thus, when plotted using a $T_{ref} = -90$ °C, the E" peak is shifted to a low frequency of ~5×10^{-6} Hz. As expected, the local motions associated with the β-relaxation dynamics are effectively frozen out at −90 °C and require long times for thermal activation. We plot the master curve shift factors (a_T) in **Figure 10B** and fit the PBDT β-relaxation shift factors with an Arrhenius equation, given as

$$\log a_T = \frac{E_a}{2.303R}\left(\frac{1}{T} - \frac{1}{T_{ref}}\right) \quad \textbf{(4)}$$

and shown as the dotted line in **Figure 10B**. The activation energy of the β-relaxation is E_a ~ 89 kJ mol^{-1}, significantly higher than typically found for simple non-cooperative β-relaxations (~40 kJ mol^{-1}), indicating a complex and cooperative relaxation process. This value is in agreement with prior studies investigating the β-relaxation of all-aromatic polyamides.[53]

The master curves for PBDT-IL composites with 20–40 wt.% PBDT are qualitatively similar to the pure polymer. However, *a priori* we know that the major component of the PBDT-IL composites is IL (60–80 wt.%) and IL dominates the thermo-mechanical response in the vicinity of the IL T_g. Thus, we assign the broad relaxation feature of the PBDT-IL composites to be a signature of the IL T_g. The intensity of the relaxation increases with decreasing polymer concentration, confirming that we are probing the IL dynamics in this range. We fit the shift factors

using the so-called Vogel-Fulcher-Tammann (VFT) law that relates the thermal dependence of the relaxation time $\tau(T)$ in the vicinity of the glass transition temperature as

$$\tau(T) = \tau_0 \exp\left(\frac{B}{T - T_\infty}\right) \quad \textbf{(5)}$$

where τ_0 is the infinite temperature relaxation time, T_∞ is the VFT divergence temperature, and B is a material specific parameter. We use an equation for fitting the a_T from TTS by taking the logarithm of the quotient $\tau(T)/\tau(T_{ref})$ and using B and T_∞ as fitting parameters. Within the framework of the VFT model, the apparent activation energy (E_g) and fragility index (m) is calculated from

$$E_g = \frac{RB}{\left(1 - T_\infty/T_g\right)} \quad \textbf{(6)}$$

$$m = \frac{B/T_g}{\ln 10 \left(1 - T_\infty/T_g\right)^2} \quad \textbf{(7)}$$

where R is the gas constant and the T_g is determined from DSC measurements. The fragility index is related to the rate of change of transport properties at temperatures close to, but above, the T_g.[56] Within this context, high and low m values indicate a fragile and strong glass former, respectively. Imidazolium-based ILs have m values in the range of 60-80, indicative of a fragile glass, i.e. the viscosity drops by many orders of magnitude as the temperature is raised through the T_g.[56] We plot the calculated E_g values in the inset of **Figure 10B** in addition to the Arrhenius E_a value of neat PBDT. We find a linear relationship between the activation energies and PBDT concentration, which suggests that the measured activation energy is a simple composite average of the IL T_g and PBDT-rich β-relaxation. The intercept value, corresponding to the E_g of pure IL, is 300 ± 5 kJ mol^{-1}, in agreement with the E_g values reported by rheometry studies on imidazolium-based ILs.[56] The calculated values of m for our PBDT-IL composites lie in the range of 0.1-10, indicating a very strong glass former. However, these calculated values are merely an apparent fragility, as the

mechanical properties of the PBDT-IL composite are dominated by the glassy polymer network at temperatures above the IL T_g.

3.7 Stress-Strain Behavior. To withstand the stresses likely to be imposed upon PEMs for use as solid-state battery electrolytes or gas separation membranes, the material should possess sufficient stiffness. In general, the addition of ILs to glassy polymer matrices results in significant plasticization and causes the tensile failure behavior to change from brittle to ductile.[29, 58] This plasticization reduces the stiffness and ultimate strength considerably, negatively impacting material properties. To investigate the effects of IL on the tensile behavior of PBDT-IL composites, we performed stress-strain measurements at 25 °C in dry conditions as shown in **Figure 11**.

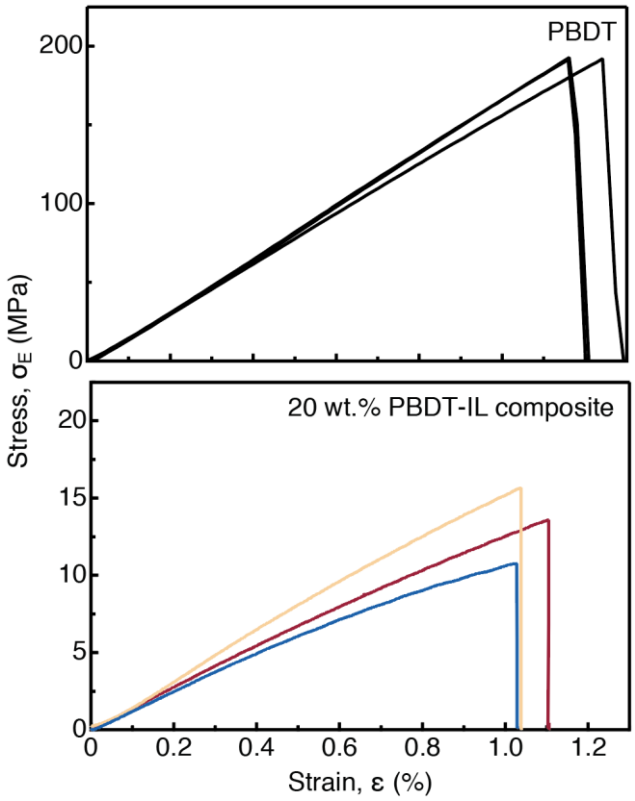

Figure 11. Stress-strain measurement in uniaxial tension for three samples of neat PBDT (*top*) and 20 wt.% PBDT-IL composite (*bottom*) at a strain rate of 1% min^{-1}. The same qualitative brittle stress-strain behavior is observed for the PBDT-IL composites as is found for neat PBDT.

Interestingly, the stress-strain behavior of the composites qualitatively matches that of the neat polymer and exhibits brittle behavior with a strain at break of ~1.1%. The ultimate strength is reduced from ~200 MPa in the neat polymer to ~13 MPa for the 20 wt.% PBDT-IL composite. This result strongly suggests that the load-bearing network structure in PBDT-IL composites remains glassy in the presence of IL and is strongly resistant to plasticization.

4.0 CONCLUSIONS

In summary, we have prepared PBDT-IL composites from a sulfo-aramid and a model IL that forms supramolecular fibrillar networks across the entire compositional range. We compared the mechanical properties and ionic conductivity of PBDT-IL composites to an exhaustive literature compilation that unambiguously demonstrates the advantage of our approach. Morphological observations utilizing optical, electron, and atomic force microscopy in conjunction with SAXS and thermo-mechanical analysis revealed a liquid crystalline, self-assembled two-phase morphology consisting of ion-conducting domains and load-bearing polymer-rich fibrils. Through SAXS, we demonstrated that the size and density of constituent fibrils within higher-order structures are modulated as a function of IL concentration with a diameter of 20−40 Å. These fibrils are highly aligned in the film plane, with an order parameter near 0.95, due to affine deformation during the membrane drying process. Thermo-mechanical measurements highlighted the best combination of room temperature modulus (0.1–2 GPa) and ion conductivity (8–4 mS cm^{-1}) of any PEM reported to date, to the best of our knowledge. Careful analysis of the thermo-mechanical data revealed a superposition of a PBDT-rich and PBDT-poor phase contributing to the mechanical relaxation spectrum, convoluted with the thermal transitions related to the pure IL. Using TTS, we extensively characterized the secondary relaxation dynamics of the PBDT-IL composites and elucidated the linear contributions of both the polymer β-relaxation and the IL glass transition to the relaxation activation energy. These new insights will guide future material design and enable the application of high-modulus and high-ion-conductivity PEMs in a variety of high-performance electrochemical and gas separation applications.

ASSOCIATED CONTENT

Supporting Information

The following files are available free of charge.

^{1}H NMR spectra of 0.1 wt.% PBDT in D_2O, TGA of PBDT and PBDT-IL composites, 3D topological AFM data, DSC scans of IL with Na^+ dopant, DSC of a 5 wt.% PBDT-IL composite either slow-cooled or quenched, WAXS of IL with Na^+ dopant, and analysis of change in E' over the IL T_g as a function of IL crystallinity.

AUTHOR INFORMATION

Corresponding Author

*E-mail: tjd@unc.edu

*E-mail: lmadsen@vt.edu

Notes

The authors declare no competing financial interests.

ACKNOWLEDGMENT

This material is based upon work supported by, or in part by, the U.S. Army Research Laboratory and the U.S. Army Research Office under contract number A17-0053-001. This work was performed in part at the Chapel Hill Analytical and Nanofabrication Laboratory (CHANL), and Duke University Shared Materials Instrumentation Facility (SMIF), members of the North Carolina Research Triangle Nanotechnology Network (RTNN) which is supported by the National Science Foundation, Grant ECCS-1542015, as part of the National Nanotechnology Coordinated

Infrastructure (NNCI). L.A.M. acknowledges the National Science Foundation under award number DMR-1810194. This work benefited from the use of the SasView application, originally developed under NSF Award DMR-0520547. SasView also contains code developed with funding from the EU Horizon 2020 programme under the SINE2020 project Grant No 654000.

REFERENCES

1. Shauser, N. S.; Harry, K. J.; Parkinson, D. Y.; Watanabe, H.; Balsara, N. P. Lithium Dendrite Growth in Glassy and Rubbery Nanostructured Block Copolymer Electrolytes. *J. Electrochem. Soc.* **2015,** *162* (3), A398-A405.
2. Lee, S.-Y.; Ogawa, A.; Kanno, M.; Nakamoto, H.; Yasuda, T.; Watanabe, M. Nonhumidified Intermediate Temperature Fuel Cells Using Protic Ionic Liquids. *J. Am. Chem. Soc.* **2010,** *132*, 9764-9773.
3. Ito, A.; Yasuda, T.; Yoshioka, T.; Yoshida, A.; Li, X.; Hashimoto, K.; Nagai, K.; Shibayama, M.; Watanabe, M. Sulfonated Polyimide/Ionic Liquid Composite Membranes for CO2 Separation: Transport Properties in Relation to Their Nanostructures. *Macromolecules* **2018,** *51* (18), 7112-7120.
4. Thakur, V. K.; Ding, G.; Ma, J.; Lee, P. S.; Lu, X. Hybrid materials and polymer electrolytes for electrochromic device applications. *Adv. Mater.* **2012,** *24* (30), 4071-4096.
5. Kikuchi, K.; Tsuchitani, S. Nafion®-based polymer actuators with ionic liquids as solvent incorporated at room temperature. *J. Appl. Phys.* **2009,** *106* (5), 053519.
6. Cho, J. H.; Lee, J.; He, Y.; Kim, B.; Lodge, T. P.; Frisbie, C. D. High-Capacitance Ion Gel Gate Dielectrics with Faster Polarization Response Times for Organic Thin Film Transistors. *Adv. Mater.* **2008,** *20*, 686-690.
7. Lodge, T. P. A Unique Platform for Materials Design. *Science* **2008,** *321*, 50-51.
8. Monroe, C.; Newman, J. The Impact of Elastic Deformation on Deposition Kinetics at Lithium/Polymer Interfaces. *J. Electrochem. Soc.* **2005,** *152* (2), A396-A404.
9. Stone, G. M.; Mullin, S. A.; Teran, A. A.; Jr., D. T. H.; Minor, A. M.; Hexemer, A.; Balsara, N. P. Resolution of the Modulus versus Adhesion Dilemma in Solid Polymer Electrolytes for Rechargeable Lithium Metal Batteries. *J. Electrochem. Soc.* **2012,** *159* (3), A222-A227.
10. Teran, A. A.; Tang, M. H.; Mullin, S. A.; Balsara, N. P. Effect of molecular weight on conductivity of polymer electrolytes. *Solid State Ionics* **2011,** *203*, 18-21.
11. Chopade, S. A.; Au, J. G.; Li, Z.; Schmidt, P. W.; Hillmyer, M. A.; Lodge, T. P. Robust Polymer Electrolyte Membranes with High Ambient-Temperature Lithium-Ion Conductivity via Polymerization-Induced Microphase Separation. *ACS Appl. Mater. Interfaces* **2017,** *9* (17), 14561-14565.
12. Schulze, M. W.; McIntosh, L. D.; Hillmyer, M. A.; Lodge, T. P. High-modulus, high-conductivity nanostructured polymer electrolyte membranes via polymerization-induced phase separation. *Nano Lett.* **2014,** *14* (1), 122-126.
13. Khurana, R.; Schaefer, J. L.; Archer, L. A.; Coates, G. W. Suppression of lithium dendrite growth using cross-linked polyethylene/poly(ethylene oxide) electrolytes: a new approach for practical lithium-metal polymer batteries. *J. Am. Chem. Soc.* **2014,** *136* (20), 7395-7402.

14. Wang, Y.; Chen, Y.; Gao, J.; Yoon, H. G.; Jin, L.; Forsyth, M.; Dingemans, T. J.; Madsen, L. A. Highly Conductive and Thermally Stable Ion Gels with Tunable Anisotropy and Modulus. *Adv. Mater.* **2016,** *28*, 2571-8.
15. Yu, Z.; He, Y.; Wang, Y.; Madsen, L. A.; Qiao, R. Molecular Structure and Dynamics of Ionic Liquids in a Rigid-Rod Polyanion-Based Ion Gel. *Langmuir* **2017,** *33* (1), 322-331.
16. Gao, J.; Wang, Y.; Norder, B.; Garcia, S. J.; Picken, S. J.; Madsen, L. A.; Dingemans, T. J. Water and sodium transport and liquid crystalline alignment in a sulfonated aramid membrane. *J. Memb. Sci.* **2015,** *489*, 194-203.
17. Sarkar, N.; Kershner, D. Rigid rod water-soluble polymers. *J. Appl. Polym. Sci.* **1996,** *62*, 393-408.
18. Lavrenko, P. N.; Okatova, O. V. Diffusion of poly(p-phenylene terephthalamide) in concentrated sulfuric acid. *Polym. Sci. U.S.S.R.* **1979,** *21*, 406-412.
19. Ilavsky, J. Nika: software for two-dimensional data reduction. *J. Appl. Cryst.* **2012,** *45*, 324-328.
20. Wang, Y.; Gao, J.; Dingemans, T. J.; Madsen, L. A. Molecular Alignment and Ion Transport in Rigid Rod Polyelectrolyte Solutions. *Macromolecules* **2014,** *47* (9), 2984-2992.
21. Wang, Y.; He, Y.; Yu, Z.; Gao, J.; Ten Brinck, S.; Slebodnick, C.; Fahs, G. B.; Zanelotti, C. J.; Hegde, M.; Moore, R. B.; Ensing, B.; Dingemans, T. J.; Qiao, R.; Madsen, L. A. Double helical conformation and extreme rigidity in a rodlike polyelectrolyte. *Nat. Commun.* **2019,** *10* (1), 801.
22. Funaki, T.; Kaneko, T.; Yamaoka, K.; Ohsedo, Y.; Gong, J. P.; Osada, Y.; Shibasaki, Y.; Ueda, M. Shear-Induced Mesophase Organization of Polyanionic Rigid Rods in Aqueous Solution. *Langmuir* **2004,** *20*, 6518-6520.
23. Every, H. A.; Mendes, E.; Picken, S. J. Ordered Structures in Proton Conducting Membranes from Supramolecular Liquid Crystal Polymers. *J. Phys. Chem. B* **2006,** *110*, 23729-23735.
24. Viale, S.; Best, A. S.; Mendes, E.; Jager, W. F.; Picken, S. J. A supramolecular nematic phase in sulfonated polyaramides. *Chem. Commun.* **2004,** *14*, 1596-1597.
25. Viale, S.; Mendes, E.; Picken, S.; Santin, O. Water Soluble Rigid Rod Polymers: A SANS Study of Shear-Induced Alignment and Relaxation. *Mol. Cryst. Liq. Cryst.* **2004,** *411* (1), 525-535.
26. Russell, H. G.; Swalen, J. D. In-plane orientation of polyimide. *J. Polym. Sci.: Polym. Phys. Ed.* **1983,** *21*, 1745-1756.
27. Mantravadi, R.; Chinnam, P. R.; Dikin, D. A.; Wunder, S. L. High Conductivity, High Strength Solid Electrolytes Formed by in Situ Encapsulation of Ionic Liquids in Nanofibrillar Methyl Cellulose Networks. *ACS Appl. Mater. Interfaces* **2016,** *8* (21), 13426-13436.
28. Yasuda, T.; Nakamura, S.-i.; Honda, Y.; Kinugawa, K.; Lee, S.-Y.; Watanabe, M. Effects of Polymer Structure on Properties of Sulfonated Polyimide/Protic Ionic Liquid Composite Membranes for Nonhumidified Fuel Cell Applications. *ACS Appl. Mater. Interfaces* **2012,** *4* (3), 1783-1790.
29. Smith, D. M.; Pan, Q.; Cheng, S.; Wang, W.; Bunning, T. J.; Li, C. Y. Nanostructured, Highly Anisotropic, and Mechanically Robust Polymer Electrolyte Membranes via Holographic Polymerization. *Adv. Mater. Interfaces* **2018,** *5* (1), 1700861.
30. Kamio, E.; Yasui, T.; Iida, Y.; Gong, J. P.; Matsuyama, H. Inorganic/Organic Double-Network Gels Containing Ionic Liquids. *Adv. Mater.* **2017,** *29* (47), 1704118.
31. Tang, B.; White, S. P.; Frisbie, C. D.; Lodge, T. P. Synergistic Increase in Ionic Conductivity and Modulus of Triblock Copolymer Ion Gels. *Macromolecules* **2015,** *48*, 4942-4950.

32. Horowitz, A. I.; Panzer, M. J. Poly(dimethylsiloxane)-supported ionogels with a high ionic liquid loading. *Angew. Chem. Int. Ed.* **2014,** *53* (37), 9780-9783.
33. Visentin, A. F.; Panzer, M. J. Poly(Ethylene Glycol) Diacrylate-Supported Ionogels with Consistent Capacitive Behavior and Tunable Elastic Response. *ACS Appl. Mater. Interfaces* **2012,** *4*, 2836-2839.
34. Fujii, K.; Asai, H.; Ueki, T.; Sakai, T.; Imaizumi, S.; Chung, U.-I.; Watanabe, M.; Shibayama, M. High-performance ion gel with tetra-PEG network. *Soft Matter* **2012,** *8*, 1756-1759.
35. Zhang, S.; Lee, K. H.; Frisbie, C. D.; Lodge, T. P. Ionic Conductivity, Capacitance, and Viscoelastic Properties of Block Copolymer-Based Ion Gels. *Macromolecules* **2011,** *44*, 940-949.
36. Henderson, K. J.; Zhou, T. C.; Otim, K. J.; Shull, K. R. Ionically Cross-Linked Triblock Copolymer Hydrogels with High Strength. *Macromolecules* **2010,** *43*, 6193-6201.
37. He, Y.; Boswell, P. G.; Buhlmann, P.; Lodge, T. P. Ion Gels by Self-Assembly of a Triblock Copolymer in an Ionic Liquid. *J. Phys. Chem. B* **2007,** *111*, 4645-4652.
38. Cho, B.-K.; Jain, A.; Gruner, S. M.; Wiesner, U., Mesophase Structure-Mechanical and Ionic Transport Correlations in Extended Amphiphilic Dendrons. *Science* **2004,** *305*, 1598-1601.
39. Wang, C.; Sakai, T.; Watanabe, O.; Hirahara, K.; Nakanishi, T. All Solid-State Lithium-Polymer Battery Using a Self-Cross-Linking Polymer Electrolyte. *J. Electrochem. Soc.* **2003,** *150* (9), A1166-A1170.
40. Lauter, U.; Meyer, W. H.; Enkelmann, V.; Wegner, G. Supramolecular structures of poly(*p*-phenylenes) with oxyethylene side chains and their mixtures with lithium salts. *Macromol. Chem. Phys.* **1998,** *199*, 2129-2140.
41. Singh, M.; Odusanya, O.; Wilmes, G. M.; Eitouni, H. B.; Gomez, E. D.; Patel, A. J.; Chen, V. L.; Park, M. J.; Fragouli, P.; Iatrou, H.; Hadjichristidis, N.; Cookson, D.; Balsara, N. P. Effect of Molecular Weight on the Mechanical and Electrical Properties of Block Copolymer Electrolytes. *Macromolecules* **2007,** *40*, 4578-4585.
42. Susan, M. A. B. H.; Kaneko, T.; Noda, A.; Watanabe, M. Ion Gels Prepared by in Situ Radical Polymerization of Vinyl Monomers in an Ionic Liquid and Their Characterization as Polymer Electrolytes. *J. Am. Chem. Soc.* **2005,** *127*, 4976-4983.
43. Glynos, E.; Papoutsakis, L.; Pan, W.; Giannelis, E. P.; Nega, A. D.; Mygiakis, E.; Sakellariou, G.; Anastasiadis, S. H. Nanostructured Polymer Particles as Additives for High Conductivity, High Modulus Solid Polymer Electrolytes. *Macromolecules* **2017,** *50* (12), 4699-4706.
44. DeVecchio, D.; Bhushan, B. Localized surface elasticity measurements using an atomic force microscope. *Review of Scientific Instruments* **1997,** *68* (12), 4498-4505.
45. Chang, K.; Luo, H.; Geise, G. M. Water content, relative permittivity, and ion sorption properties of polymers for membrane desalination. *J. Membr. Sci.* **2019,** *574*, 24-32.
46. Solveyra, E. G.; de la Llave, E.; Scherlis, D. A.; Molinero, V. Melting and crystallization of ice in partially filled nanopores. *J. Phys. Chem. B* **2011,** *115* (48), 14196-204.
47. Higuchi, A.; Iijima, T. D.s.c investigation of the states of water in poly(vinyl alcohol-co-itaconic acid) membranes. *Polymer* **1985,** *26*, 1833-1837.
48. Ward, I. M.; Sweeney, J. *An Introduction to the Mechanical Properties of Solid Polymers, 2nd Ed.* John Wiley & Sons, Ltd: 2004.
49. Teixeira, J. Small-Angle Scattering by Fractal Systems. *J. Appl. Cryst.* **1988,** *21*, 781-785.
50. Zhang, F.; Ilavsky, J. Ultra-Small-Angle X-ray Scattering of Polymers. *Polym. Rev.* **2010,** *50* (1), 59-90.

51. Picken, S. J.; Aerts, J.; Visser, R.; Northolt, M. G. Structure and rheology of aramid solutions-X-ray scattering measurements. *Macromolecules* **1990,** *23*, 3849-3854.
52. Shimomura, T.; Takamuku, T.; Yamaguchi, T. Clusters of imidazolium-based ionic liquid in benzene solutions. *J. Phys. Chem. B* **2011,** *115* (26), 8518-27.
53. Frosini, V.; Butta, E. Some Remarks on the Mechanical Relaxations in Aliphatic, Partially Aromatic, and Wholly Aromatic Polyamides. *Polym. Lett.* **1971,** *9*, 253-260.
54. Tao, R.; Simon, S. L. Rheology of Imidazolium-Based Ionic Liquids with Aromatic Functionality. *J. Phys. Chem. B* **2015,** *119*, 11953-11959.
55. Pogodina, N. V.; Nowak, M.; Läuger, J.; Klein, C. O.; Wilhelm, M.; Friedrich, C. Molecular Dynamics of Ionic Liquids as Probed by Rheology. *J. Rheol.* **2011,** *55* (241), 241-255.
56. Shamim, N.; McKenna, G. B. Glass Dynamics and Anomalous Aging in a Family of Ionic Liquids above the Glass Transition Temperature. *J. Phys. Chem. B* **2010,** *114*, 15742-15752.
57. Graessley, W. W.; Edwards, S. F. Entanglement interactions in polymers and the chain contour concentration. *Polymer* **1981,** *22*, 1329-1334.
58. Xu, D.; Wang, B.; Wang, Q.; Gu, S.; Li, W.; Jin, J.; Chen, C.; Wen, Z. High-Strength Internal Cross-Linking Bacterial Cellulose-Network-Based Gel Polymer Electrolyte for Dendrite-Suppressing and High-Rate Lithium Batteries. *ACS Appl. Mater. Interfaces* **2018,** *10* (21), 17809-17819.

PROPOSED TOC Graphic: for Table of Contents use only